LETTER

doi:10.1038/nature17149

The past, present and future of African dust

Amato T. Evan[1,2], Cyrille Flamant[2], Marco Gaetani[2] & Françoise Guichard[3]

African dust emission and transport exhibits variability on diurnal[1] to decadal[2] timescales and is known to influence processes such as Amazon productivity[3], Atlantic climate modes[4], regional atmospheric composition and radiative balance[5] and precipitation in the Sahel[6]. To elucidate the role of African dust in the climate system, it is necessary to understand the factors governing its emission and transport. However, African dust is correlated with seemingly disparate atmospheric phenomena, including the El Niño/Southern Oscillation[7,8], the North Atlantic Oscillation[9], the meridional position of the intertropical convergence zone[10,11], Sahelian rainfall[8] and surface temperatures over the Sahara Desert[12], all of which obfuscate the connection between dust and climate. Here we show that the surface wind field responsible for most of the variability in North African dust emission reflects the topography of the Sahara, owing to orographic acceleration of the surface flow. As such, the correlations between dust and various climate phenomena probably arise from the projection of the winds associated with these phenomena onto an orographically controlled pattern of wind variability. A 161-year time series of dust from 1851 to 2011, created by projecting this wind field pattern onto surface winds from a historical reanalysis[13], suggests that the highest concentrations of dust occurred from the 1910s to the 1940s and the 1970s to the 1980s, and that there have been three periods of persistent anomalously low dust concentrations—in the 1860s, 1950s and 2000s. Projections of the wind pattern onto climate models give a statistically significant downward trend in African dust emission and transport as greenhouse gas concentrations increase over the twenty-first century, potentially associated with a slow-down of the tropical circulation. Such a dust feedback, which is not represented in climate models, may be of benefit to human and ecosystem health in West Africa via improved air quality[14] and increased rainfall[6]. This feedback may also enhance warming of the tropical North Atlantic[15], which would make the basin more suitable for hurricane formation and growth[16].

We perform an eigenanalysis of zonal and meridional wind speeds at 10 m above the surface from the European Centre for Medium-Range Weather Forecasts Interim reanalysis product[17] (ERA-I) to identify coherent variability in wind fields associated with dust emission and transport (see Methods). Most relevant to this study is the second empirical orthogonal function (EOF) and corresponding principal component (PC) time series from the eigenanalysis of 10-m winds (Fig. 1a), which explains approximately 20% of the variance in the data (EOFs and PCs for the first and third modes are shown in Extended Data Fig. 1). The spatial structure of the second EOF maximizes in the region of 15° N and 10°–20° E, with secondary maxima extending towards the northwest (Fig. 1a). The wind fields in this EOF exhibit a northeasterly flow across much of the Sahara, characteristic of the trade winds, as well as a westerly flow near 30° N and 0° E.

The corresponding second PC time series (PC2) has a maximum in the 1980s, which is followed by a steep decline over the following decade (Fig. 1b). From 2000 through to the end of the record, values for the ERA-I PC2 largely remain between 0 and −1 standard deviations. The time series of ERA-I PC2 is strikingly similar to that of dust optical depth over the Cape Verde islands (15° N, 23.5° W) retrieved from the Advanced Very High Resolution Radiometer (AVHRR) space-borne imager[2]. We average over this area in order to compare to coral proxy data[2], but note that dust over Cape Verde is highly representative of dust over the entire tropical North Atlantic[2] and our results are qualitatively identical if we instead average the AVHRR data over the entire tropical North Atlantic. In Fig. 1b both monthly time series are smoothed with a 13-month running mean filter to highlight variability on interannual and longer time scales. The correlation between the ERA-I PC2 and AVHRR dust smoothed time series is 0.76 ($P \approx 0.01$; all P values reported here account for time series autocorrelation). The ERA-I wind fields and dust retrievals from the AVHRR are independent, so the fact that ERA-I PC2 explains 58% of the variance in the AVHRR dust data is strong evidence that dust emission and transport, on these temporal and spatial scales, can also be approximated as a linear function of surface wind speeds over the Sahara (see Methods and Extended Data Fig. 2).

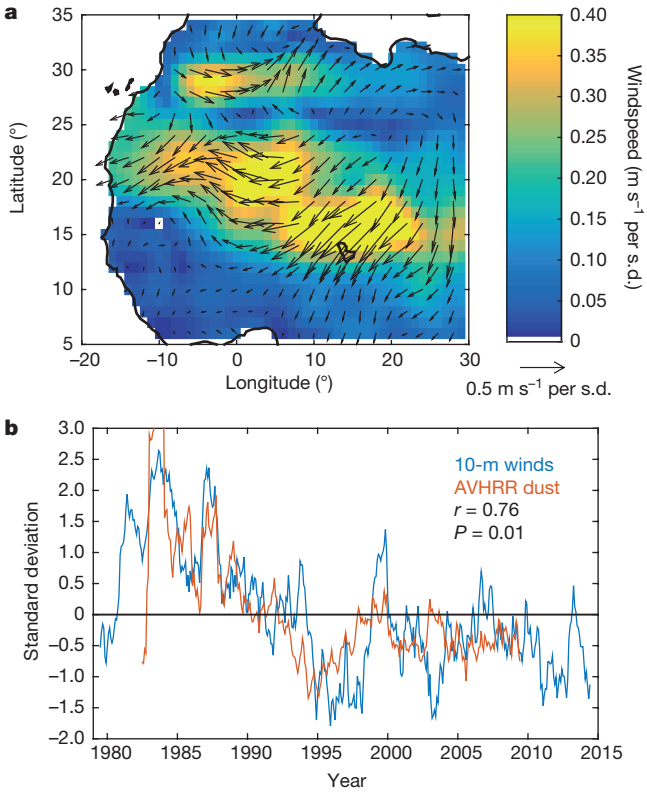

Figure 1 | Second EOF/PC of North African 10-m winds. a, The spatial structure of the second EOF of 10-m winds over North Africa. Arrows and shading represent the direction and magnitude of monthly mean winds, respectively, in units of wind speed per unit standard deviation (s.d.) change in the PC time series. **b**, The associated PC time series (10-m winds) and a time series of dust optical depth averaged over the tropical North Atlantic (AVHRR dust). The second EOF/PC explains 15% of the total variance in the surface winds data.

[1]Scripps Institution of Oceanography, University of California, San Diego, La Jolla, California, USA. [2]Laboratoire Atmosphères, Milieux, Observations Spatiales (LATMOS)/IPSL, UPMC Université Paris 06, Sorbonne Université, UVSQ, CNRS, Paris, France. [3]CNRM-GAME, UMR 3589 CNRS and Météo-France, Toulouse, France.

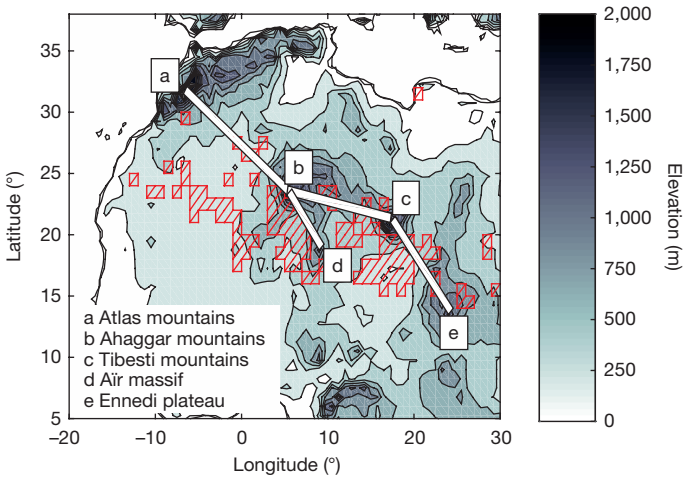

Figure 2 | North African orography and dust source regions. Shading represents surface elevation and transects indicate regions where orography increases the magnitude of the surface wind speed; the relevant topographic features are indicated in the legend and the surface altitude along each transect is shown in Extended Data Fig. 3. The red-hatched regions encompass the major Saharan dust sources[20].

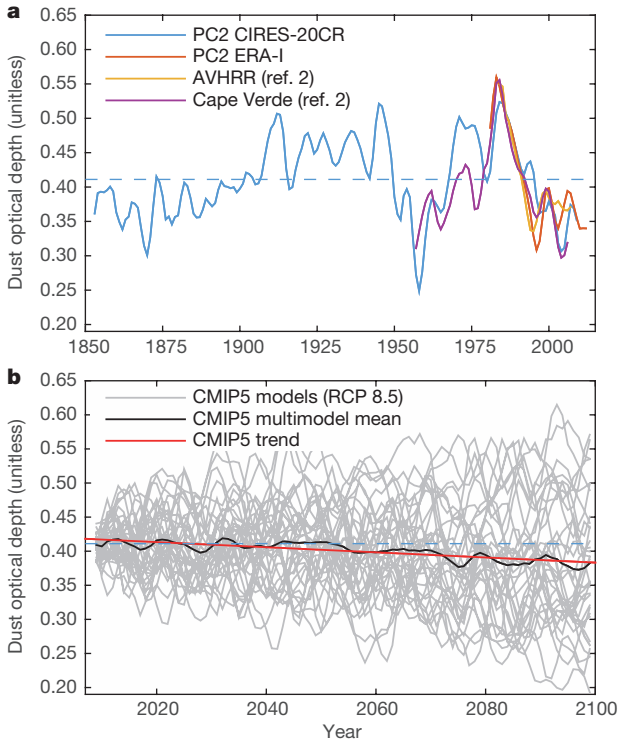

Figure 3 | Estimates of North Atlantic dust. a, PC2 time series from the CIRES-20CR and ERA-I reanalyses, and the AVHRR and hybrid satellite-coral (Cape Verde) dust time series. The ERA-I PC2 data are scaled to be in units of dust optical depth in a manner identical to that for the CIRES-20CR PC2 time series. **b**, The CMIP5 ensemble mean PC2 time series, the multimodel mean CMIP5 PC2 time series and its linear trend. The dashed blue lines are the long-term mean of the CIRES-20CR PC2 time series. Annual mean time series are smoothed with a 1-4-6-4-1 filter.

The spatial structure of the second EOF (Fig. 1a) closely resembles the topography over the Sahara (Fig. 2). In particular, the wind vectors exhibit a maximum in magnitude downstream of the gaps between the major Saharan mountains and plateaus, which are indicated by the transect lines and labels a–e (surface elevations are shown for each transect in Extended Data Fig. 3). It is not surprising that this EOF of 10-m winds reflects surface topography; flow acceleration at the exit region of a gap results in an increase of the variance of the down-gap winds, relative to variance of the up-gap, non-accelerated winds[18]. This similarity in the spatial structure of the second EOF and the orography of the Sahara, and the high correlation between the PC2 and the AVHRR dust time series, are both consistent with previous work showing that most dust emitted from the Sahara is generated within major topographic depressions[19]. According to a recent study[20], approximately 85% of all North African dust emission occurs within the areas indicated with blue hatching, which are generally downwind of the gaps indicated in Fig. 2, and which encompasses the regions where the magnitude of the second EOF is high.

We next project the spatial structure of the second EOF (Fig. 1a) onto the NOAA-CIRES 20th Century Reanalysis[21] (CIRES-20CR) monthly mean 10-m wind fields to recreate a historical proxy record of dust emission and westward transport over the Atlantic. We convert the units of the CIRES-20CR PC2 time series to dust optical depth by linearly scaling the CIRES-20CR PC2 time series so that its standard deviation and mean are identical to that from the AVHRR data over their common time period of 1982–2009 (blue line in Fig. 3a). The CIRES-20CR PC2 time series is highly correlated with the ERA-I PC2 series (orange line in Fig. 3a) at an r value of 0.63 ($P < 0.01$), the AVHRR dust optical depth time series (yellow line in Fig. 3a) at $r = 0.54$ ($P < 0.02$), and a 54-year dust proxy dust time series based on AVHRR data and other data from a Cape Verde coral[2] (purple line) at $r = 0.55$ ($P < 0.01$). These r and P values were calculated using unsmoothed annual time series.

The positive and statistically significant correlations between the CIRES-20CR PC2 time series and the other dust time series in Fig. 3a are evidence that this record of over 150 years can be used to study historical North African dust emission and transport. Over the entire CIRES-20CR PC2 time series, there are two relatively persistent periods of increased dustiness, 1910–1950 and 1970–1990, and three periods of low dust concentrations, the mid-1860s to early 1870s, 1950 to the late 1960s, and the last 15 years of the record. There is not a secular trend in dust emission and transport over the entire record, but there are coherent multi-decadal trend periods, including upward trends from 1870–1910 and the late 1950s to the mid-1980s, and downward trends from the mid-1940s to 1960 and the mid-1980s to the end of the record. In addition, the variance of the first half of the CIRES-20CR PC2 time series (4.9×10^{-3}) is 58% of the variance of the second half of the record (8.4×10^{-3}), raising the possibility that anthropogenic forcing has caused an enhancement in year-to-year changes in the amount of dust emitted from North Africa.

Our results suggest that any phenomenon that excites surface winds over North Africa in a manner that projects onto the spatial structure in Fig. 1a will influence the net production and transport of Saharan dust. Such a theory reconciles the disparity of published work on the controls on North African dust production and suggests that, to first order, to understand dust variability one needs only to elucidate the factors that excite the pattern of surface wind speeds in Fig. 1a. Our results explain why although time series of dust are correlated with a diversity of climate phenomena, these correlations are not stationary in time. For example, an analysis of correlation coefficients between different climate indices and CIRES-20CR PC2, for a moving 31-year window, suggests that the high dust emissions of the 1910s and 1940s were related to the phase of the North Atlantic Oscillation, but that the high dust emissions of the 1980s were associated with the Sahelian drought (Extended Data Fig. 4).

We next examine simulated changes in African dust during the twenty-first century using output from the Fifth Climate Model Intercomparison Project (CMIP5, Extended Data Table 1). As CMIP5 models are unable to reproduce observed twentieth-century changes in African dust[22] we estimate future dustiness by projecting the EOF pattern in Fig. 1 onto the monthly mean 10-m wind fields for these models. We first consider winds from the so-called 'business-as-usual' scenario (RCP 8.5), in which emissions of greenhouse gases continue to increase throughout the twenty-first century[23]. We convert ensemble mean CMIP5 PC2 time series to unit dust optical depth by scaling each series so that its standard deviation is equal to the standard deviation of the entire CIRES-20CR PC2 time series (Fig. 3b).

We also offset each model's mean optical depth so that the mean of the first five model years (2005–2010) is equal to 0.4, the long-term mean of the CIRES-20CR PC2 time series (blue dashed line, Fig. 3b).

The twenty-first-century CMIP5 PC2 time series for each model is a typical 'spaghetti plot' (grey lines in Fig. 3b), reflecting the models' internal variability; the range of individual model dust optical depth values is 0.2 to 0.6. The CMIP5 multimodel mean time series (thick black line) shows a statistically significant downward trend of -0.04 ± 0.01 (in units of dust optical depth) per 100 years (red line in Fig. 3b). This 100-year change is approximately 40% of the magnitude of the models' standard deviation over the same period and represents a 10% reduction in the CIRES-20CR PC2 long-term mean dust optical depth. Furthermore, 15 of the 34 models considered here have statistically significant downward trends in dust optical depth yet only six models have statistically significant upward trends in dust optical depth (Extended Data Fig. 5a). We repeated this analysis for the RCP 4.5 simulations, in which emissions of greenhouse gases peak during 2040–2050, finding a statistically significant downward trend in dust optical depth of -0.02 ± 0.01, half of that for the RCP 8.5 simulation (Extended Data Fig. 5b). The multimodel mean time series from the RCP scenarios represent an estimate of the response of dust to increasing levels of greenhouse gasses and do not reflect other sources of variability.

From our analysis of the CMIP5 data we conclude that the future reduction in emission and transport of dust from Africa is a robust response to increasing greenhouse gas emissions. The CMIP5 trends were not sensitive to the types of aerosol indirect effects included in the model, suggesting that the trend is not related to twenty-first-century changes in the concentration of atmospheric aerosols included in the simulations. We estimate the 'time of emergence' of the greenhouse gas forced trend to be 200 years ($P = 0.05$) based on bootstrap resampling tests using noise characteristics from the CIRES-20CR PC2 time series (see Methods), and thus the trend in the CMIP5 multimodel mean is consistent with the lack of a trend over the entire CIRES-20CR PC2 time series (Fig. 3). However, there is a statistically significant downward trend in CIRES-20CR PC2 over the twentieth century (-0.08 ± 0.06 per 100 years). It is plausible that the twentieth- and twenty-first-century PC2 downward trends are associated with a slow-down of the tropical circulation[24].

This decline in dust over North Africa may result in a slight improvement in air quality in the region, although the effect of regional population growth and urbanization will undoubtedly overshadow the benefits of a reduction in airborne dust[25]. While the radiative forcing of dust may be near zero over North Africa, as shortwave cooling is approximately balanced by the longwave warming[6], dust transported over the tropical North Atlantic cools the surface via direct[2,15] and indirect[26] radiative effects. Therefore, a reduction in dust would act as a positive feedback to warming by greenhouse gases in the tropical North Atlantic. Furthermore, since this feedback is not pan-tropical, this additional dust-forced warming could increase hurricane activity by increasing tropical North Atlantic sea surface temperature[27], relative sea surface temperature (which is the difference between sea surface temperature in the tropical Atlantic and the sea surface temperature averaged over all of the tropics[28]), and the northward meridional sea surface temperature gradient[4,29]. The radiative and temperature effects from such a reduction in dust are not captured in most CMIP5 simulations; many models do not have interactive dust, and of those models that do, the majority show an increase in simulated African dust concentrations during the twenty-first century (Extended Data Fig. 6). Thus, it is plausible that current temperature projections for the tropical Atlantic through the Caribbean are too conservative.

Online Content Methods, along with any additional Extended Data display items and Source Data, are available in the online version of the paper; references unique to these sections appear only in the online paper.

Received 5 October 2015; accepted 11 January 2016.

1. Chaboureau, J. P., Tulet, P. & Mari, C. Diurnal cycle of dust and cirrus over West Africa as seen from Meteosat Second Generation satellite and a regional forecast model. *Geophys. Res. Lett.* **34,** L02822 (2007).
2. Evan, A. T. & Mukhopadhyay, S. African dust over the northern tropical Atlantic: 1955–2008. *J. Appl. Meteorol. Climatol.* **49,** 2213–2229 (2010).
3. Bristow, C. S., Hudson-Edwards, K. A. & Chappell, A. Fertilizing the Amazon and equatorial Atlantic with West African dust. *Geophys. Res. Lett.* **37,** L14807 (2010).
4. Evan, A. T., Foltz, G. R., Zhang, D. & Vimont, D. J. Influence of African dust on ocean-atmosphere variability in the tropical Atlantic. *Nature Geosci.* **4,** 762–765 (2011).
5. Ridley, D. A., Heald, C. L. & Prospero, J. M. What controls the recent changes in African mineral dust aerosol across the Atlantic? *Atmos. Chem. Phys.* **14,** 5735–5747 (2014).
6. Yoshioka, M. *et al.* Impact of desert dust radiative forcing on Sahel precipitation: relative importance of dust compared to sea surface temperature variations, vegetation changes, and greenhouse gas warming. *J. Clim.* **20,** 1445–1467 (2007).
7. DeFlorio, M. J. *et al.* Interannual modulation of subtropical Atlantic boreal summer dust variability by ENSO. *Clim. Dyn.* **46,** 585–599 (2015).
8. Prospero, J. M. & Lamb, P. J. African droughts and dust transport to the Caribbean: climate change implications. *Science* **302,** 1024–1027 (2003).
9. Moulin, C. *et al.* Control of atmospheric export of dust from North Africa by the North Atlantic Oscillation. *Nature* **287,** 691–694 (1997).
10. Doherty O. M., Riemer N. & Hameed S. Control of Saharan mineral dust transport to Barbados in winter by the Intertropical Convergence Zone over West Africa. *J. Geophys. Res.* **117,** D19117 (2012).
11. Doherty, O. M., Riemer, N. & Hameed, S. Role of the convergence zone over West Africa in controlling Saharan mineral dust load and transport in the boreal summer. *Tellus B* **66,** 23191 (2014).
12. Wang, W. J., Evan, A. T., Flamant, C. & Lavaysse, C. On the decadal scale correlation between African dust and Sahel rainfall: the role of Saharan heat low-forced winds. *Science Adv.* **1,** e1500646 (2015).
13. Compo, G. P. *et al.* The twentieth century reanalysis project. *Q. J. R. Meteorol. Soc.* **137,** 1–28 (2011).
14. Griffin, D. W. & Kellogg, C. A. Dust storms and their impact on ocean and human health: dust in Earth's atmosphere. *EcoHealth* **1,** 284–295 (2004).
15. Evan, A. T., Vimont, D. J., Heidinger, A. K., Kossin, J. P. & Bennartz, R. The role of aerosols in the evolution of tropical North Atlantic ocean temperature anomalies. *Science* **324,** 778–781 (2009).
16. Dunion, J. P. & Velden, C. S. The impact of the Saharan air layer on Atlantic tropical cyclone activity. *Bull. Am. Meteorol. Soc.* **85,** 353–365 (2004).
17. Dee, D. P. *et al.* The ERA-Interim reanalysis: configuration and performance of the data assimilation system. *Q. J. R. Meteorol. Soc.* **137,** 553–597 (2011).
18. Washington, R. *et al.* Links between topography, wind, deflation, lakes and dust: the case of the Bodélé depression, Chad. *Geophys. Res. Lett.* **33,** L09401 (2006).
19. Prospero, J. M., Ginoux, P., Torres, O., Nicholson, S. E. & Gill, T. E. Environmental characterization of global sources of atmospheric soil dust identified with the Nimbus 7 Total Ozone Mapping Spectrometer (TOMS) absorbing aerosol product. *Rev. Geophys.* **40,** 1002 (2002).
20. Evan, A. T. *et al.* Derivation of an observation-based map of North African dust emission. *Aeolian Res.* **16,** 153–162 (2015).
21. Compo, G. P. *et al.* The twentieth century reanalysis project. *Q. J. R. Meteorol. Soc.* **137,** 1–28 (2011).
22. Evan, A. T., Flamant, C., Fiedler, S. & Doherty, O. An analysis of aeolian dust in climate models. *Geophys. Res. Lett.* **41,** 5996–6001 (2014).
23. Taylor, K. E., Stouffer, R. J. & Meehl, G. A. An overview of CMIP5 and the experiment design. *Bull. Am. Meteorol. Soc.* **93,** 485–498 (2012).
24. Held, I. M. & Soden, B. J. Robust responses of the hydrological cycle to global warming. *J. Clim.* **19,** 5686–5699 (2006).
25. Liousse, C. *et al.* Explosive growth in African combustion emissions from 2005 to 2030. *Environ. Res. Lett.* **9,** 035003 (2014).
26. Doherty, O. M. & Evan, A. T. Identification of a new dust-stratocumulus indirect effect over the tropical North Atlantic. *Geophys. Res. Lett.* **41,** 6935–6942 (2014).
27. Emanuel, K. A. Increasing destructiveness of tropical cyclones over the past 30 years. *Nature* **436,** 686–688 (2005).
28. Vecchi, G. A. & Soden, B. J. Effect of remote sea surface temperature change on tropical cyclone potential intensity. *Nature* **450,** 1066–1070 (2007).
29. Kossin, J. P. & Vimont, D. J. A more general framework for understanding Atlantic hurricane variability and trends. *Bull. Am. Meteorol. Soc.* **88,** 1767–1781 (2007).

Acknowledgements This work was supported by the Agence Nationale de la Recherche (ANR) grant ANR-10-LABX-18-01 of the national Programme Investissements d'Avenir provided by the Laboratoire d'excellence Institut Pierre Simon Laplace (L-IPSL). We appreciate comments from our colleagues.

Author Contributions A.T.E. carried out the main analysis and wrote the manuscript. F.G. analysed wind speed data from weather stations. All authors designed the study, discussed the results and commented on the manuscript.

Author Information Reprints and permissions information is available at www.nature.com/reprints. The authors declare no competing financial interests. Readers are welcome to comment on the online version of the paper. Correspondence and requests for materials should be addressed to A.T.E. (aevan@ucsd.edu).

METHODS

EOF and PC calculations. To calculate the EOFs of 10-m winds over North Africa we removed the mean and seasonal cycle from the monthly mean zonal and meridional wind fields from ERA-I for the period 1979–2014. ERA-I contains global atmospheric parameters from January 1979 to the present, at T255 spectral resolution (approximately 80 km). We spatially smoothed the monthly mean data via a uniformly weighted 3° × 3° filter and divided the data into subsets from −20° to 30° E and 2° to 35° N, with over-water values masked out. Eigenvectors were calculated from these smoothed and subsetted fields. The PC time series were calculated by projecting the subsequent eigenvalues back onto the data, and the EOF spatial pattern (Fig. 1a) is the regression of the meridional and zonal wind fields onto the PC time series. The PC time series for the CIRES-20CR (Fig. 3a) was calculated by smoothing and subsetting the CIRES-20CR 10-m zonal and meridional wind fields in a manner identical to that done for the ERA-I data. We then projected the second eigenvector from the ERA-I EOF analysis (Fig. 1) onto the CIRES-20CR wind fields to derive an equivalent PC time series for the CIRES-20CR data set.

We repeated the eigenanalysis of 10-m winds using other reanalysis products, including the NOAA-CIRES Twentieth-Century Reanalysis[13], the ERA Twentieth-Century Reanalysis[31], the NASA Modern-Era Retrospective analysis for Research and Applications[32], the NCEP-DOE AMIP-II Reanalysis[33] and the NCEP NCAR Reanalysis[34] (Extended Data Fig. 7). While the results from the eigenanalysis of these other reanalysis products show elements of the second EOF from ERA-I, these were mixed among the first two or three EOFs, and rotation of the EOFs did not clearly separate out the dust signal as is seen in the ERA-I data (Fig. 1b).

Recent work has shown that, when compared to observations of surface winds from meteorological stations across the Sahel, 10-m winds from ERA-I are more accurate than those from other reanalyses[30]. We expanded on the analysis in ref. 30 to include stations in the Sahara, also finding that here 10-m winds from ERA-I were more accurate than those from other reanalysis products (Extended Data Fig. 8).

We also examined the PC2 time series from the CMIP5 historical forcing experiments. These CMIP5 PC2 time series for individual models are constructed in a manner identical to that for the RCP 8.5 simulations in Fig. 3. The resultant multimodel mean time series had a standard deviation approximately 20% of that from the CIRES-20CR, and thus to facilitate comparison between the two we scaled the multimodel mean time series to have a standard deviation equal to that of the CIRES-20CR time series (Extended Data Fig. 9). The CIRES-20CR and the CMIP5 multimodel mean show some agreement in their trends, including a rise in dust emission and transport from 1880 to 1930 and a reduction in dust over the end of the record.

Variability in the multimodel mean historical forcing simulations should reflect external forcing only, that is, associated with variations in solar insolation, greenhouse gases or aerosol concentrations but not internal variability of the climate system. Thus, disagreement between the two time series may be due to a combination of internal variability of the physical climate system and poor representation of key processes controlling surface winds over North Africa on these timescales, where the latter may also be a major reason why the variance in the multimodel mean time series was one-fifth of that from CIRES-PC2.

Linearization of the relationship between wind speed and dust emission. The results in Fig. 1b suggest that monthly mean dust emission and transport is, to first order, linearly proportional to monthly mean surface wind speed. Such an assumption is common, although often implicit, when examining the interannual variability of dust (for example, refs 9–12), which may be unexpected given that dust emission is proportional to the cube of wind speed (for example, ref. 35). To test this assumption we analysed hourly data from three synoptic stations in the Sahara that are close to the major dust source regions (Djanet and Tamanrasset in Algeria and Agadez in Niger). We calculated the so-called dust uplift potential (DUP)[36] using the characteristic emission threshold of 6 m s^{-1} (refs 37–39). From the hourly data we calculated the monthly mean wind speed and the monthly mean DUP. At each station DUP is highly correlated with wind speed, with r values ranging from 0.86 (Djanet) to 0.93 (Agadez) and P values < 0.01 (Extended Data Fig. 2). These results demonstrate that on monthly and longer timescales the monthly mean dust emission is, to first-order, proportional to monthly mean wind speed.

As another test of the linearity assumption, and to remove potential biases related to seasonality of series autocorrelation, for each station we randomly drew 24 × 30 wind speed samples from the data set (representing a month of hourly wind speed observations), calculated the DUP, and then averaged these DUP and wind speed values. We repeated this procedure 100 times and calculated the correlation between the randomly sampled wind speed and DUP values, finding qualitatively similar r and P values for correlations between this monthly mean DUP and the measured wind speed at each station (not shown). We repeated this procedure, increasing the sampling to 1000 and 10,000, obtaining similar results with both (not shown). As a final test of the linearity assumption, we fitted the wind speed distribution for each station to a lognormal distribution, randomly sampled then averaged the distributions in a manner identical to that described above, and then calculated the pseudo monthly mean values of DUP and wind speed. The resultant correlation coefficients between DUP and wind speed were also qualitatively similar (not shown).

Although local changes in soil moisture and vegetation do influence dust emission[37,40], our results suggest that variability in North African dust emission and transport is little affected by such properties of the surface. This is because the main dust source regions (Fig. 2) are within the hyper-arid Sahara (defined as a mean annual rainfall of less than 100 mm), where soil moisture and vegetation are extremely limited (for example, ref. 41). The negligible influence of soil moisture and vegetation to the interannual variability of North African dust is consistent with recent modelling work[5] as well as previous studies on the factors governing the interannual variability of dust (for example, refs 9–12).

Time of emergence. The time of emergence of the PC2 trends is an estimate of the length of the time series required to detect a trend at 95% confidence level, which we determined via a bootstrap method. To do so we created 1000 random (normal) time series of length 500 years with standard deviation equal to that of the CIRES-20CR PC2 time series (Fig. 3a) and a linear trend equal to that of the RCP 8.5 multimodel mean (Extended Data Fig. 5a). We calculated the linear least-squares trend and the 95% confidence interval on the trend for the time series using the first 2 years, then the first 3 years, then the first 4 years, through to 500 years. The time of emergence is then calculated as the length of the time series for which the trend is statistically different from zero at the 95% confidence interval, which in this case is 195 years.

Data. CMIP5 data are available through the Earth System Grid (http://pcmdi9.llnl.gov/). Satellite and proxy dust data are available through the PANGAEA Data Publisher for Earth and Environmental Science (http://doi.pangaea.de/10.1594/PANGAEA.855141) and a map of North African dust emission is available from the same resource at http://doi.pangaea.de/10.1594/PANGAEA.855243. ERA-I and ERA Twentieth-Century Reanalysis data are available from the European Centre for Medium-Range Weather Forecasts (ERA-20CR) (http://www.ecmwf.int/). CIRES-20CR, DOE AMIP-II (NCEP2) and NCEP NCAR (NNRP) Reanalysis data are from the Earth System Research Laboratory (http://www.esrl.noaa.gov/). NASA Modern-Era Retrospective analysis for Research and Applications (MERRA) data are from the Goddard Earth Sciences Data and Information Services Center (http://disc.sci.gsfc.nasa.gov). Wind speed data from Saharan synoptic weather stations are from the Wyoming Weather Web (http://weather.uwyo.edu) and the AMMA database (http://database.amma-international.org). The Niño 3.4 time series and Palmer Drought[42,43] data are available from the NOAA Climate Prediction Center (http://www.cpc.ncep.noaa.gov). Jones North Atlantic Oscillation[44] data are from the UK Climate Research Unit (http://www.cru.uea.ac.uk/). The Saharan Heat Low thickness time series is calculated using ERA-I data via the methodology in ref. 45 and data on the latitude of the intertropical convergence zone are calculated using NNRP data via the methodology in ref. 10.

Code availability. The codes used to conduct the analysis presented in this paper and in the production of the figures are available at https://github.com/amatoevan/2015DUST/.

30. Largeron, Y. *et al.* Can we use surface wind fields from meteorological reanalyses for Sahelian dust emission simulations? *Geophys. Res. Lett.* **42,** 2490–2499 (2015).
31. Dee, D., Balmaseda, D. M., Balsamo, G., Engelen, R. & Simmons, A. Toward a consistent reanalysis of the climate system. *Bull. Am. Meteorol. Soc.* **95,** 1235–1248 (2014).
32. Rienecker, M. M. *et al.* MERRA: NASA's modern-era retrospective analysis for research and applications. *J. Clim.* **24,** 3624–3648 (2011).
33. Kanamitsu, M. *et al.* NCEP-DOE AMIP-II reanalysis (R-2). *Bull. Am. Meteorol. Soc.* **83,** 1631–1643 (2002).
34. Kalnay, E. *et al.* The NCEP/NCAR 40-year reanalysis project. *Bull. Am. Meteorol. Soc.* **77,** 437–471 (1996).
35. Marticorena, B. & Bergametti, G. Modeling the atmospheric dust cycle: 1. Design of a soil-derived dust emission scheme. *J. Geophys. Res.* **100,** 16415–16430 (1995).
36. Marsham, J. H., Knippertz, P., Dixon, N. S., Parker, D. J. & Lister, G. M. S. The importance of the representation of deep convection for modeled dust-generating winds over West Africa during summer. *Geophys. Res. Lett.* **38,** L16803 (2011).
37. Cowie, S. M., Knippertz, P. & Marsham, J. H. Are vegetation-related roughness changes the cause of the recent decrease in dust emission from the Sahel? *Geophys. Res. Lett.* **40,** 1868–1872 (2013).

38. Westphal, D. L., Toon, O. B. & Carlson, T. N. A two-dimensional numerical investigation of the dynamics and microphysics of Saharan dust storms. *J. Geophys. Res.* **92,** 3027–3049 (1987).
39. Tegen, I. & Fung, I. Modeling of mineral dust in the atmosphere: sources, transport, and optical thickness. *J. Geophys. Res.* **99,** 22897–22914 (1994).
40. Fécan, F., Marticorena, B. & Bergametti, G. Parameterization of the increase of the aeolian erosion threshold wind friction velocity due to soil moisture for arid and semi-arid areas. *Ann. Geophys.* **17,** 149–157 (1999).
41. Washington, R., Todd, M. C., Engelstaedter, S., Mbainayel, S. & Mitchell, F. Dust and the low-level circulation over the Bodélé Depression, Chad: observations from BoDEx 2005. *J. Geophys. Res.* **111** (D3), D03201 (2006).
42. Dai, A., Trenberth, K. E. & Qian, T. A global data set of Palmer Drought Severity Index for 1870-2002: relationship with soil moisture and effects of surface warming. *J. Hydrometeorol.* **5,** 1117–1130 (2004).
43. Mahowald, N. M. *et al.* Observed 20th century desert dust variability: impact on climate and biogeochemistry. *Atmos. Chem. Phys.* **10,** 10875–10893 (2010).
44. Jones, P. D., Jonsson, T. & Wheeler, D. Extension to the North Atlantic Oscillation using early instrumental pressure observations from Gibraltar and South-West Iceland. *Int. J. Climatol.* **17,** 1433–1450 (1997).
45. Lavaysse, C. *et al.* Seasonal evolution of the West African heat low: a climatological perspective. *Clim. Dyn.* **33,** 313–330 (2009).

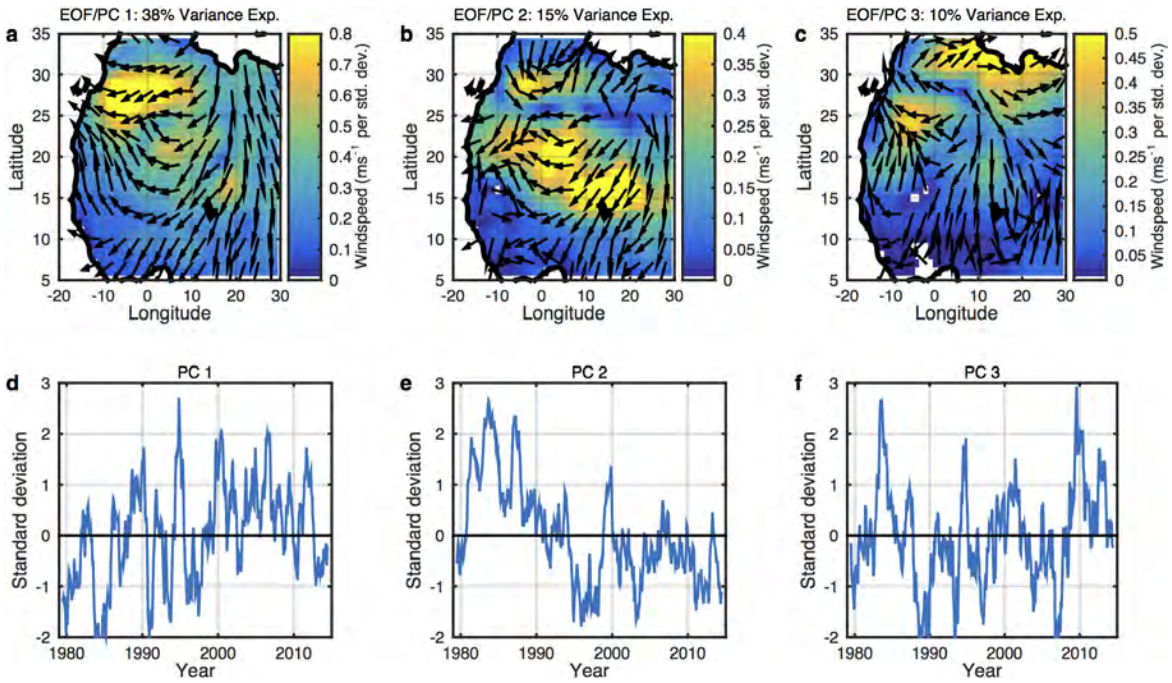

Extended Data Figure 1 | First three EOFs and PCs of 10-m winds over North Africa from ERA-I. Shown is the spatial structure of the first three EOFs from the eigenanalysis of monthly mean 10-m winds from ERA-I (**a**–**c**), and the corresponding PC time series in units of standard deviation (**d**–**f**). Descriptions of arrows, shading and time series are identical to that for Fig. 1. See Methods for details of the eigenanalysis.

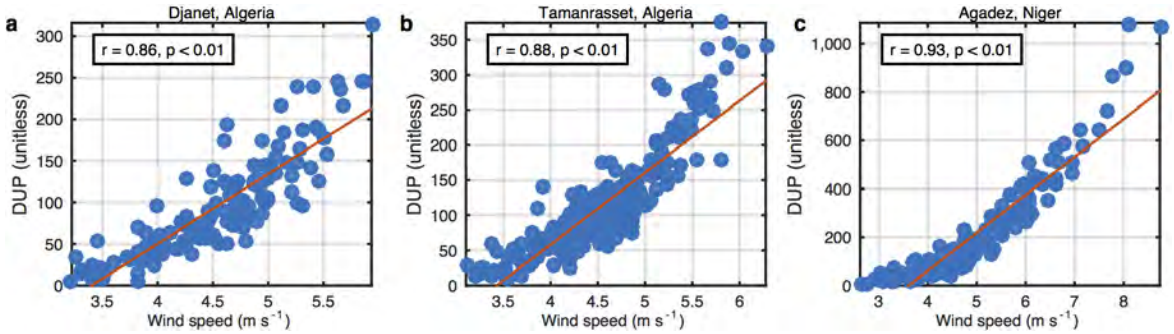

Extended Data Figure 2 | Comparison of monthly mean wind speeds and dust uplift potential. Shown are scatter plots (blue filled circles) of mean monthly DUP (ordinate axis) and wind speeds (abscissa axis) for the North African synoptic stations at Djanet, Algeria (**a**), Tamanrasset, Algeria (**b**) and Agadez, Niger (**c**). Also shown for reference are the least-squares best-fit lines (red). The correlation coefficient *r* and statistical significance *P* are indicated in each plot.

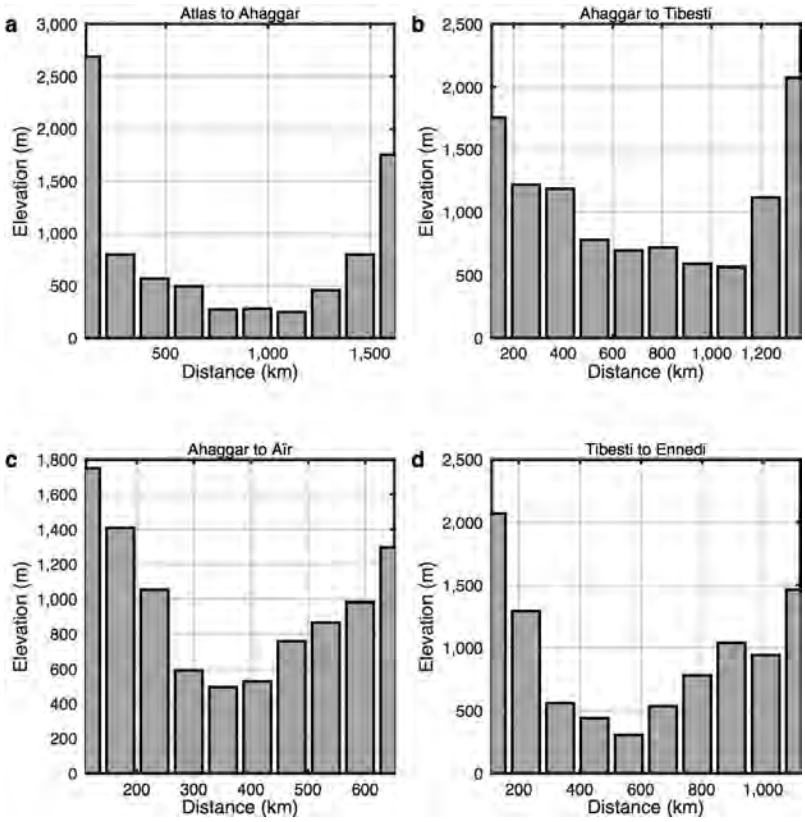

Extended Data Figure 3 | Topography affecting surface winds across the Sahara. Shown are surface elevations along each transect in Fig. 2: the Atlas to the Ahaggar mountains (**a**), the Ahaggar to the Tibesti mountains (**b**), the Ahaggar mountains to the Aïr massif (**c**) and the Tibesti mountains to the Ennedi plateau (**d**). These topographic features accelerate the surface flow and give rise to the spatial structure of the second EOF and PC pair (Fig. 1a). The titles indicate the major topographic features bounding each transect. Note the different horizontal lengths (abscissa) and heights (ordinate) for each plot.

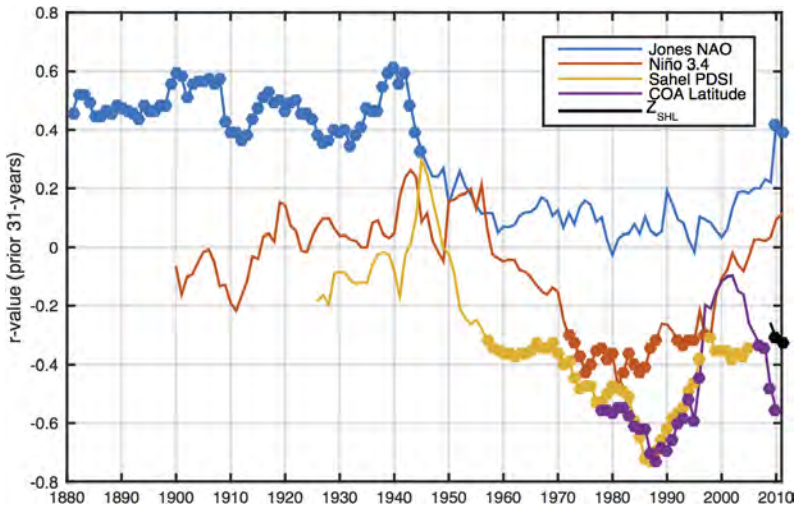

Extended Data Figure 4 | Non-stationary correlations between CIRES-20CR PC2 and climate indices. Plotted is the correlation coefficient between the annual mean CIRES-20CR PC2 and the Jones North Atlantic Oscillation, Niño 3.4, the Sahel-averaged Palmer Drought Severity index (PDSI), the latitude of the intertropical convergence zone, and the 925–700 hPa thickness of the Saharan Heat Low (Z_{SHL}). All correlation coefficients are for the preceding 31-year period (for example, the value of 0.6 for the Jones North Atlantic Oscillation in 1940 indicates that the correlation coefficient between the Jones North Atlantic Oscillation and the CIRES-20CR PC2 is 0.6 for the period 1910–1940). We indicate statistically significant correlations ($P < 0.05$) with a filled circle, although here the P value is not calculated using effective degrees of freedom (as is the case elsewhere in this Letter).

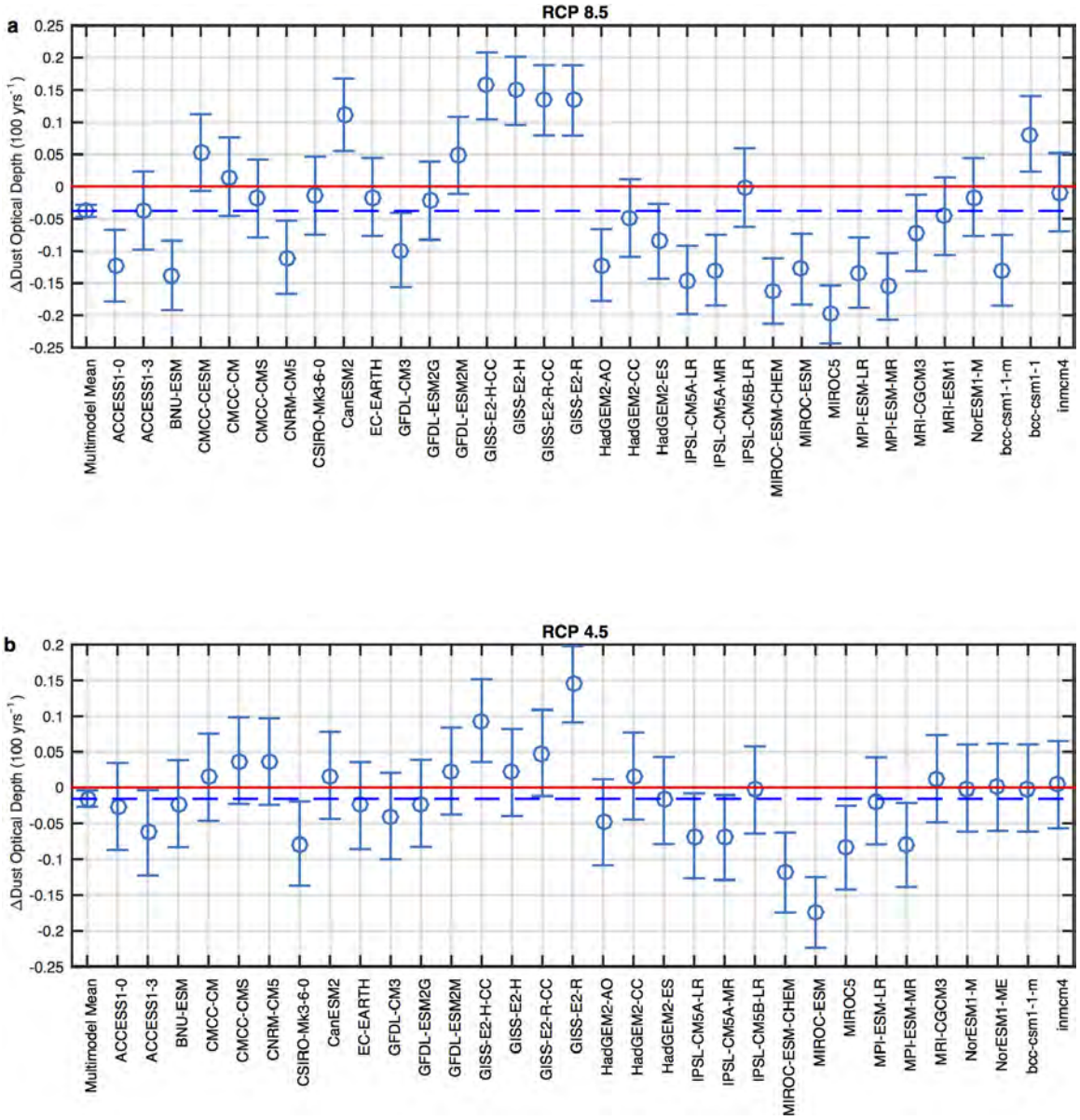

Extended Data Figure 5 | CMIP5 RCP 4.5 and RCP 8.5 twenty-first-century trends in PC2. a, RCP 8.5. **b**, RCP 4.5. Shown are the PC2 linear trends (circles), 95% confidence intervals (error bars) and the multimodel mean trend (blue dashed line) for RCP 8.5 (top) and 4.5 (bottom) simulations. All trends are in units of dust optical depth per 100 years.

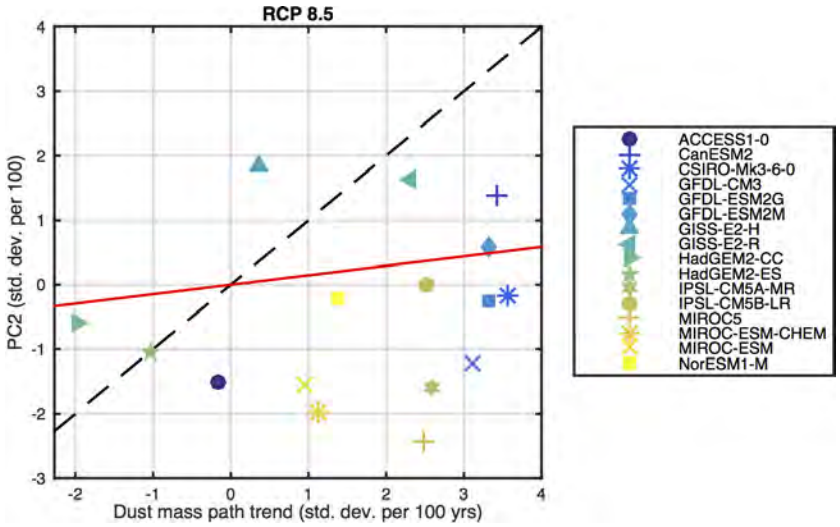

Extended Data Figure 6 | CMIP5 RCP 8.5 twenty-first-century trends in estimated and modelled dust. Plotted is the CMIP5 models' twentieth-century trends in dust mass path for the RCP 8.5 experiments (abscissa) versus the twentieth-century trends calculated from the PC2 time series (ordinate). Included here are only CMIP5 models for which dust mass path and 10-m wind data are available. The red line is the least-squares best-fit line (slope is not statistically different from zero) and the dashed line is the one-to-one line. All trends are in units of standard deviation per 100 years.

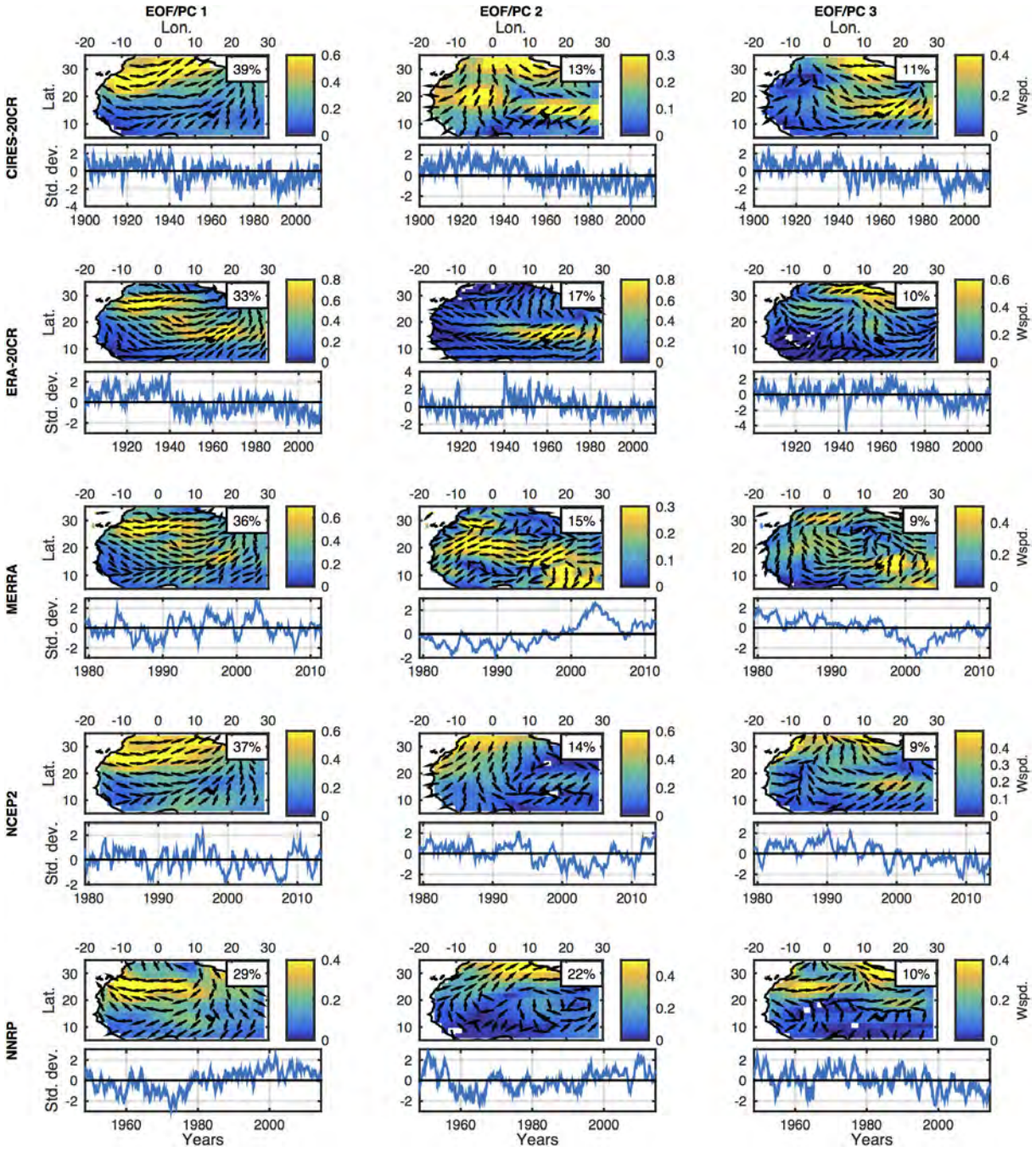

Extended Data Figure 7 | EOF/PC pairs for various reanalyses. Shown are the first three EOFs (top rows) and corresponding PC time series (bottom rows) calculated from the CIRES-20CR, ERA-20CR, MERRA, NCEP2 and NNRP data sets. Percentages of the variance of the data set explained by each EOF/PC pair are shown.

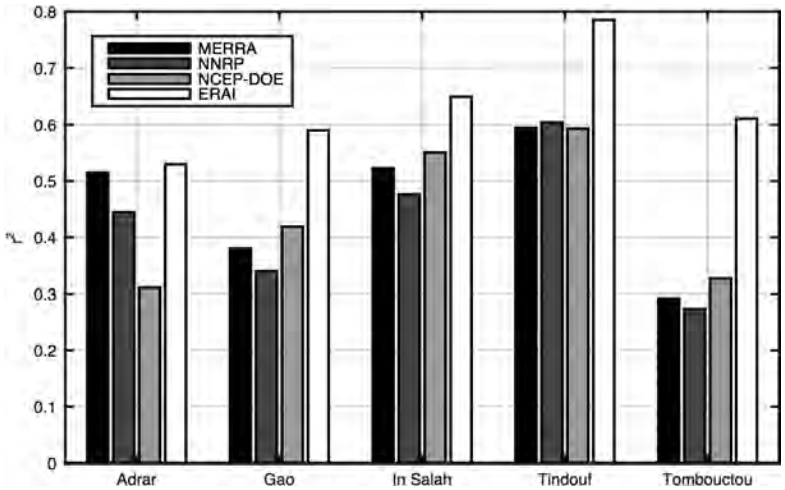

Extended Data Figure 8 | Wind speed comparisons between observations and reanalyses. Shown are the r^2 values from the correlation between monthly mean surface winds from station data and monthly mean 10-m winds from reanalyses for five stations in the Sahara over the period 2000–2013. In all cases the r^2 values for ERA-I are greater than 0.5 and higher than those for the other reanalyses.

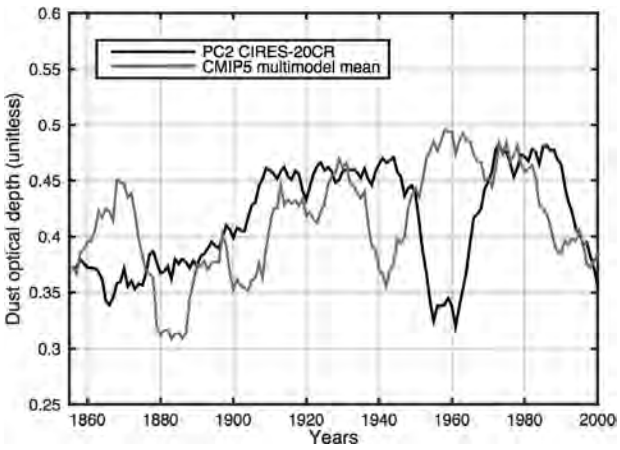

Extended Data Figure 9 | Modelled and reanalysis time series of historical dust. Plotted is the PC2 time series from the CIRES-20CR, identical to that shown in Fig. 3a, and the CMIP5 multimodel mean PC2 time series from the historical forcing simulations. Both annul mean time series have been smoothed with an 11-point running mean filter to highlight decadal scale variability.

Extended Data Table 1 | CMIP5 models used in this study

Institution	Model	Historical	RCP4.5	RCP8.5
Commonwealth Scientific and Industrial Research Organisation (CSIRO) and Bureau of Meteorology (BOM; Australia)	ACCESS1.0	3	1	1
	ACCESS1.3	3	1	1
Beijing Climate Center (BCC; China)	BCC-CSM1.1	0	0	1
	BCC-CSM1.1(m)	0	1	1
Global Change and Earth System Science (GCESS), Beijing Normal University (BNU; China)	BNU-ESM	1	1	1
Canadian Centre for Climate Modelling and Analysis (CCCma; Canada)	CanESM2	5	5	5
Centro Euro-Mediterraneo per I Cambiamenti Climatici (CMCC; Italy)	CMCC-CESM	1	0	1
	CMCC-CM	1	1	1
	CMCC-CMS	1	1	1
Centre National de Recherches Météorologiques (CNRM)–Centre Européen de Recherche et de Formation Avancée en Calcul Scientifique (CERFACS; France)	CNRM-CM5	9	1	4
CSIRO–Queensland Climate Change Centre of Excellence (QCCE; Australia)	CSIRO-Mk3.6.0	0	9	9
European consortium (EC)	EC-EARTH	1	3	2
National Oceanographic and Atmospheric Administration (NOAA) Geophysical Fluid Dynamics Laboratory (GFDL; United Stated)	GFDL-CM3	0	1	1
	GFDL-ESM2G	0	0	1
	GFDL-ESM2M	0	1	1
National Aeronautics and Space Administration (NASA) Goddard Institute for Space Studies (GISS; United Stated)	GISS-E2-H-CC	0	1	1
	GISS-E2-H	6	5	2
	GISS-E2-R-CC	0	1	1
	GISS-E2-R	6	6	2
National Institute of Meteorological Research (NIMR)–Korea Meteorological Administration (KMA; South Korea)	HadGEM2-AO	0	1	1
Met Office Hadley Centre (MOHC; United Kingdom)	HadGEM2-CC	0	1	1
	HadGEM2-ES	0	4	4
Institute for Numerical Mathematics (INM; Russia)	INM-CM4	1	1	1
L'Institut Pierre-Simon Laplace (IPSL; France)	IPSL-CM5A-LR	6	3	3
	IPSL-CM5A-MR	3	1	1
	IPSL-CM5B-LR	1	1	1
Model for Interdisciplinary Research on Climate (MIROC; Japan)	MIROC5	0	3	3
	MIROC-ESM	3	1	1
	MIROC-ESM-CHEM	1	1	1
Max Planck Institute for Meteorology (MPI-M; Germany)	MPI-ESM-LR	3	3	3
	MPI-ESM-MR	3	3	1
Meteorological Research Institute (MRI; Japan)	MRI-CGCM3	5	1	1
	MRI-ESM1	0	0	1
Norwegian Climate Centre (NCC; Norway)	NorESM1-M	3	1	1
	NorESM1-ME	1	1	0

Shown are the modelling centres, model names, and the number of ensemble members for both RCP experiments and the historical forcing experiment examined in this study.